LETTER

Experimental simulation of materials degradation of plasma-facing components using lasers

N. Farid[1,2], S.S. Harilal[1], O. El-Atwani[1], H. Ding[2] and A. Hassanein[1]

[1] Center for Materials Under Extreme Environment, School of Nuclear Engineering, Purdue University, West Lafayette, IN 47907, USA
[2] School of Physics and Optical Engineering, Key Laboratory of Materials Modification by Laser, Ion and Electron Beams, Dalian University of Technology, Dalian, People's Republic of China

E-mail: hassanein@purdue.edu

Abstract
The damage and erosion of plasma-facing components (PFCs) due to extremely high heat loads and particle bombardment is a key issue for the nuclear fusion community. Currently high current ion and electron beams are used in laboratories for simulating the behaviour of PFC materials under ITER-like conditions. Our results indicate that high-power nanosecond lasers can be used for laboratory simulation of high heat flux PFC material degradation. We exposed tungsten (W) surfaces with repetitive laser pulses from a nanosecond laser with a power density $\sim$ a few GW cm^{-2}. Emission spectroscopic analysis showed that plasma features at early times followed by intense particle emission at later times. Analysis of laser-exposed W surface demonstrated cracks and grain structures. Our results indicate that the typical particle emission features from laser-irradiated tungsten are consistent with high-power particle beam simulation results.

Keywords: plasma-facing components (PFCs), ITER, tungsten, surface erosion

(Some figures may appear in colour only in the online journal)

1. Introduction

Currently extensive laboratory-scale studies are undergoing to investigate the erosion and degradation of plasma-facing component (PFC) materials for successful operation of ITER-like fusion devices. Due to higher energy loads to the diverter surfaces during ITER operation, the surface of PFC will be exposed to extremely large fluences of hydrogen, helium and radiating impurities [1]. Therefore, erosion and sputtering of PFCs under such a higher particle flux and power loads during the steady state and edge localized modes (ELMs) can affect the performance of ITER [2]. Melting, melt motion, evaporation and splashing are the main erosion mechanisms happening during the high-power transient events [3, 4]. W has been selected as a PFC material in the activated phase of ITER and currently suggested as a first wall material in DEMO. High melting point and thermal conductivity and low erosion rate and low tritium inventory are the major advantages

of W material, which makes it suitable for plasma fusion technology [5]. On the other hand, ductile-to-brittle transition is also a major drawback of W, which could produce large macroscopic particles as well as small dust particles. The emission of dust particles from W is found to persist for longer duration compared with plasma lifetime with velocities of several tens m s^{-1} [6]. The melt motion and capillary effects cause the bridge formation and such bridges generate nano- to submicrometre size dust particles during the interaction with the next pulses [7]. Therefore, further studies related to degradation and erosion of W PFC material is important because these particles and dust grains can be transported in the fusion vessel and then in the plasma core which will significantly affect ITER operation [8, 9].

Currently sophisticated ion or electron beam facilities are routinely used for simulating ITER-like conditions in the laboratory for studying the damage and erosion of PFC materials. Our studies show that high-power lasers can be
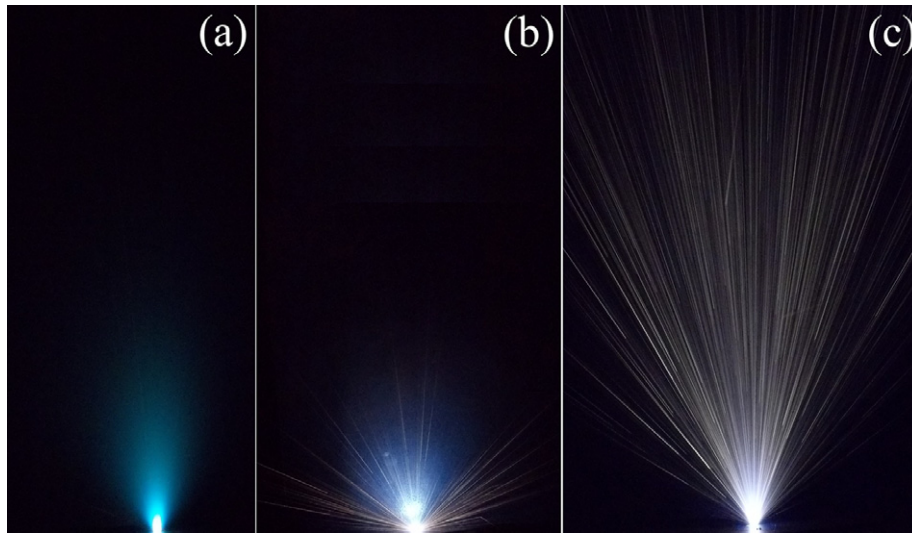
Figure 1. Time-integrated images of emission from W target after laser exposure of 0.46 MJ m^{-2} are given for different power loads. A 2 ms time integration was used for recording the images. (*a*) Image of the plasma after the first shot, (*b*) stream of ejected particles after $\sim$50 pulses and (*c*) stream of ejected particles after $\sim$100 pulses.

used for simulating similar features in the laboratory. Lasers are versatile sources of transient energy with a multitude of flexible parameters. Due to its potential advantages, the fusion community has developed an interest in employing laser-based techniques for *in situ* diagnostic of the fuel retention, compositional and cleaning of deposited layers on the first wall and PFC in fusion reactors [10–14]. In this study, we exposed the W surface with high-power laser pulses for investigating the use of a laser as an energy source to simulate the behaviour of PFC materials under highly transient loads. Our present results highlight that the surface morphology, as well as particle emission after high-power laser exposure to W PFC material, showed similarity to the ion beam interaction with W target.

2. Experimental setup

A neodymium-doped yttrium aluminum garnet (Nd : YAG) laser operating at 1064 nm and at 10 Hz repetition rate was used to expose a polycrystalline cold-rolled W (99.95% purity, average grain size $\sim$1 μm) provided by Alfa Aesar. The laser gives 6 ns full-width at half-maximum (FWHM) pulses and possesses an approximately Gaussian profile. The whole experiments were performed in a high vacuum chamber with a base pressure of $\sim$10^{-6} Torr. To provide a fresh W surface for each measurement, the target was mounted on an *XY* translational stage. The laser beam was allowed to pass through a window of the chamber and focused perpendicularly on the sample surface using a plano-convex lens (f = 40 cm) with spot diameter $\sim$500 μm. The fluence at the target surface was set at $\sim$0.46 MJ m^{-2} ($\sim$7.6 GW cm^{-2}) for the entire experiments. A complementary metal–oxide–semiconductor (CMOS) sensor camera with 2 ms exposure per frame was used to record time-integrated emission of particle streams. The time evolution of plasma self-emission and the particle distribution were collected by fast-gated imaging setup comprising of an intensified charged coupled device (ICCD) camera. The spectral emission features of the particles were analysed using a 0.5 m triple grating

(1800, 600 and 150 lines mm^{-1}) spectrograph, which was coupled to an ICCD. To analyse the particle size and their distribution from the W surface, a polish silicon substrate was placed at a distance of 12 cm and was characterized using an atomic force microscope (AFM). Surface morphology of the treated samples was characterized by utilizing scanning electron microscope (SEM). Cross-sectional imaging of the exposed sample was performed using a dual beam focused ion beam/SEM and secondary electron images were taken using the electron beam.

3. Results and discussion

Tungsten surface was exposed with repetitive laser pulses at an energy load $\sim$0.46 MJ m^{-2}. As in ITER, during type-I ELMs the energy flux of several MJ m^{-2} is typically expected which is deposited during a transient event (0.1–1 ms). Although, the laser fluence is comparable to the energy load during the ELMs, it has to be mentioned that ELM duration is several orders of magnitude longer than the laser pulse used in the present studies, which resulted in lower power density. However, we used 1064 nm laser excitation for this study and hence the majority of the laser energy will be coupled to the plasma rather than the target material after the plasma generation. Previous laser breakdown studies showed that nearly 90% of the energy will be absorbed by the plasma after its generation [15], which is consistent with the recent modelling results of plasma shielding during laser exposure [16]. Hence the energy density coupled to the target will considerably be less than the given value. Even though the power density used in this study is higher than compared with the anticipated values in ITER, the present results could be useful for the investigation of PFC erosion and material degradation during the abnormal events under ELM-like transients and high-energy loads.

Figure 1 shows the time-integrated particle emission recorded during the laser interaction with the polycrystalline W with an integration time of 2 ms. It should be noted that there were no particle emissions during the first few pulses as
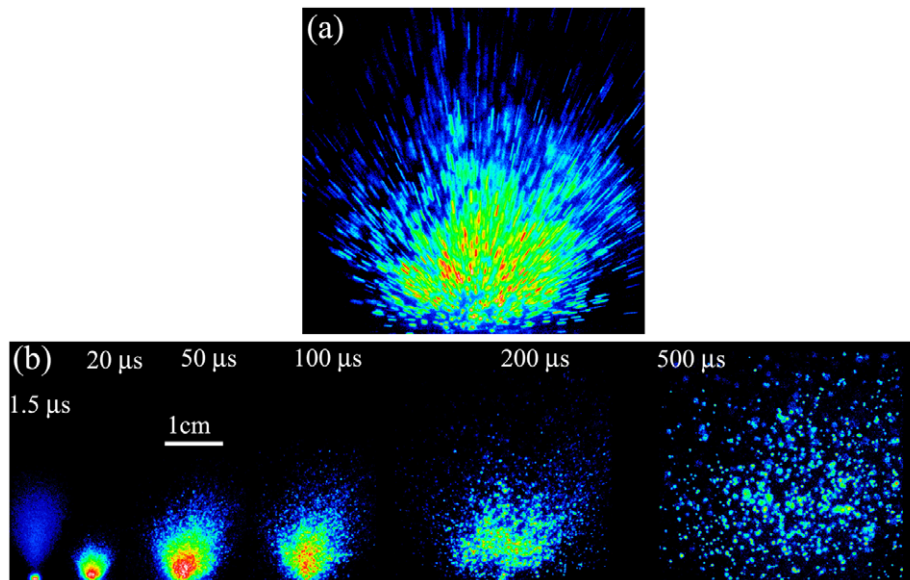
Figure 2. W plume/particle images recorded at different times using an ICCD after the laser pulses are given; (*a*) time-integrated with an integration time 2 μs and delay 100 μs and (*b*) time-resolved traces of tungsten particles obtained using 500 ns gate width.

shown in figure 1(*a*). Particle emission started after loading the tungsten surface with repetative laser pulse exposure. At 0.46 MJ m^{-2} energy load, particle emission started after about ∼50 pulses with higher flux at large angles to the target normal, as shown in figure 1(*b*). The number of emitted particles increases with a higher flux emerging normal to the target surface with further exposure of the W surface with subsequent laser pulses, as shown in figure 1(*c*). With increasing energy load the particle emission is found to appear earlier (results not given). It indicates that preconditioning of the target surface is necessary to observe firework-like emission of particles. The preconditioning becomes faster with increasing energy load.

We evaluated temporal emission features of particle emission using an ICCD. The ICCD provides a 2D view of 3D plume expansion and particle emission features and provides useful information about hydrodynamics. Figure 2(*a*) shows the stream of particles acquired using an integration time of 2 μs and with a delay of 100 μs while figure 2(*b*) shows the time-resolved particle emission captured at various times after laser exposure. For time-resolved studies, the gate width of the camera exposure was set at 500 ns for each frame. The particle emission features were observed even after 500 μs after the termination of the laser pulse. Particles continue to be ejected from the surface after the laser impact and their velocity can be estimated from the length of their traces. An average velocity of 50 ms^{-1} was derived from the particle movement in a direction perpendicular to the target surface. Similar particle emission features were reported previously from carbon and carbon-based materials during intense transient heat loads generated by electron beams as well as by lasers [17–19]. The mechanism of particle generation was attributed to the brittle destruction of carbon at an elevated temperature.

Spectroscopic studies showed that in the early times, typical line emission from W plasma was evident along with plasma continuum. The plasma bremsstrahlung occurs when a free electron collides with another particle and makes transition to another free state of lower energy with an emission of a photon. With time, the line-to-continuum ratio increases and finally, the spectrum consists of mainly ionic and atomic lines. However, the line emission disappeared after about ∼1 μs delay but there exists strong continuum thermal (blackbody) emission from the particles. The evolution of the particle movement at different time delays and distances and their temperature can be measured from their blackbody emission features. By taking into account the particle emissivity and the CCD detector photon counts, under the assumption of $hc/\lambda \gg KT$, the emission intensity I is given by [20]

$$I(\lambda) \propto \lambda^{-5} \exp\left(-\frac{hc}{\lambda k_{\mathrm{B}} T}\right)$$

where λ (μm) is the wavelength; h, k_{B} and c are the Plank and Boltzmann constants, and the speed of light, respectively. The slope of semi-logarithmic plot of $I\lambda^5$ against $1/\lambda$ is equal to $hc/k_{\mathrm{B}}T$. A typical normalized broadband continuum emission spectrum and semi-logarithmic plot corrected for the spectral response of the detection system are given in figures 3(*a*) and (*b*), respectively.

The temperature estimate of the particles showed that they possess higher temperatures at early times with a maximum recorded temperature ∼4300 K at 1 μs, but rapidly cools down to ∼2400 K at 10 μs. The temperature curve with time showed a t^{-1} dependence (curve fit in figure 3(*b*)). The melting and evaporation temperatures of W are 3687 K and 5828 K, respectively. At early times (∼1 μs), the estimated particle temperature is higher than the melting point of W which could be due to the contribution by the hot droplet splashing from molten material.

Surface morphology of the treated W surfaces has been performed using SEM in order to get better insight into various mechanisms leading to particle generation. As the emission from particles starts after a certain number of laser pulses, it can be concluded that the surface structures on the irradiated area could play a vital role in the generation of the particles. Figure 4(*a*) presents the surface morphology of the
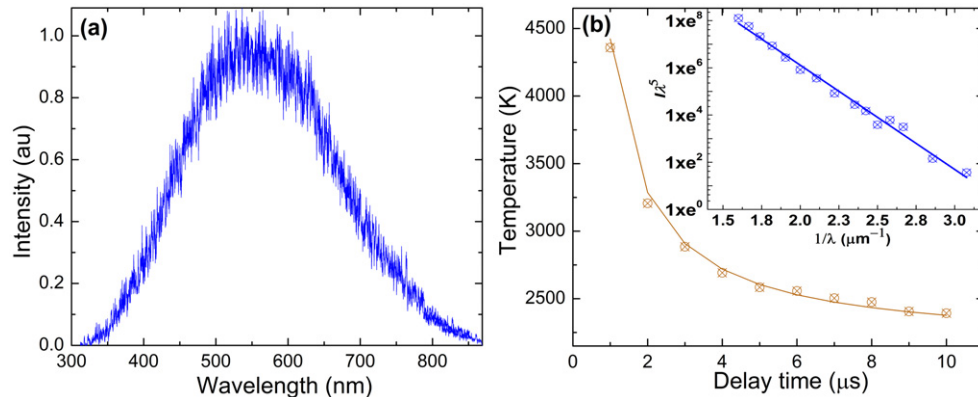
Figure 3. A typical spectrum of thermal emission from particles recorded after $10\,\mu$s delay with a gate width of $1\,\mu$s and at a distance $2\,$mm from the target surface and (*b*) variation in particle temperature with delay time with respect to laser peak (distance $= 2\,$mm). The solid curve corresponds to t^{-1} fitting. The inset of (*b*) shows the typical semi-logarithmic plot of $I\lambda^5$ against $1/\lambda$ after spectral response correction (distance $2\,$mm, time delay $2\,\mu$s).

irradiated tungsten surface after 50 laser shots with a laser energy density of $\sim 0.46\,$MJ$\,$m^{-2}. SEM micrographs clearly indicate that the energy load was sufficient to provide melting. The SEM micrographs permit measurement of crater aperture sizes and observation of the molten material which has been re-solidified in and around the central melting region. The laser-treated area can be divided into the central melting pool and a region around it where the melting material solidified in the form of microstructures. The ridge formation with melted whirlpools or channels around the central portion, turbulence with liberation of micrometre-sized particulates, droplets and cracks can be seen in the treated surface. Considering the Gaussian nature of the pulse shape, the intensity will be maximum at the centre and decreases towards the periphery. Hence it generates a temperature gradient, which causes liquid material movement mainly along the radial direction resulting in the formation of a regular ridge around the crater which spreads to the periphery of the irradiated spot. Moreover, the pressure gradient above the exposed surface from the evaporated material can cause this as well. At a similar range of energy density, the melting and vapour shielding has also been observed both with plasma and H ion beam irradiation [6, 7, 19, 20, 21]. It has been reported that during ion beam surface modification of W under the melting threshold heat load can lead to ductile-to-brittle transition and to the formation of surface cracks, which produced large dust particles of up to $30\,\mu$m [21]. However, irradiation with energy load above the melting threshold leads to recrystallization of molten material resulting in the brittleness of W [22]. Therefore, the formation of fine cracks along the grain boundaries in the re-solidified melting material is the main source of generation of nano-to-micrometre size particles [23, 24].

There exists some controversy about the mechanisms of particle generation during high heat flux exposure to the W surface. For example in [25], the W surface was irradiated with heat load higher than the melting threshold using a plasma gun. They explained that particle emission is caused by Kelvin–Helmholtz instability due to the splashing of melted material and boiling of superheated W liquid after plasma pressure drop. On the other hand, the ductile-to-brittle transition effect of tungsten produces cracks, which could also be responsible for

the generation of particles. As in [21], the heat load above the cracking threshold was applied and concluded that ejected particles from the surface is due to crack development and major crack bifurcation.

The nature of the cracks observed on the treated surfaces is evident in the surface and cross-sectional SEM images. Figure 4(*b*) shows a crack near the molten region with a varying width that ranges from 150 to 550 nm. A zoomed region (figure 4(*c*)) indicates that the crack occurred through a recrystallized region of ultrafine grains ($<500\,$nm) [26]. Figure 4(*d*) confirms the same observation outside the molten region. The majority of the cracks are on the molten region or in the periphery. Moreover, figures 4(*c*) and (*d*) demonstrate that the cracks which occurred through the grain boundaries were intergranular in nature, which is a sign of brittle destruction behaviour in tungsten. Cross-sectional imaging of the cracks shows a crack depth of a few micrometres (figures 4(*e*) and (*f*)) in the middle of the molten region. Tungsten exposed to severe heat load, typical for ITER type-I ELMS, demonstrated that the crack formation behaviour is of intergranular nature [27, 28]. Garkusha *et al* [27] ran an ELM I type relevant plasma heat load experiment on tungsten that resulted in the formation of fine and large cracks. While the formation of fine cracks was believed to be a result of the generated thermal stresses on the loaded surface, ductile-to-brittle transition effects were correlated with the formation of large cracks. Hirai *et al* [28] conjectured that the thermal stresses cause fine crack formation in severe heat loaded tungsten. Pestchanyi *et al* [29] demonstrated that two types of thermal stresses are generated on ELM-relevant heat loaded tungsten. The first type is the compressive stress due to the temperature gradient between the heat loaded surface and the cooled bulk, and the second type is the tensile stress due to cooling down of the re-solidified melted surface. The tensile stresses were described to be more important in the development of cracks. If these tensile stresses exceed the tensile stress of the material, cracks will be generated. With the power loads we had in this study, both kinds of stresses are applicable. Moreover, as mentioned earlier, the Gaussian nature of the pulse causes pressure and temperature gradients along the radial direction. Therefore, crack formation can be enhanced due to the repetitive energy
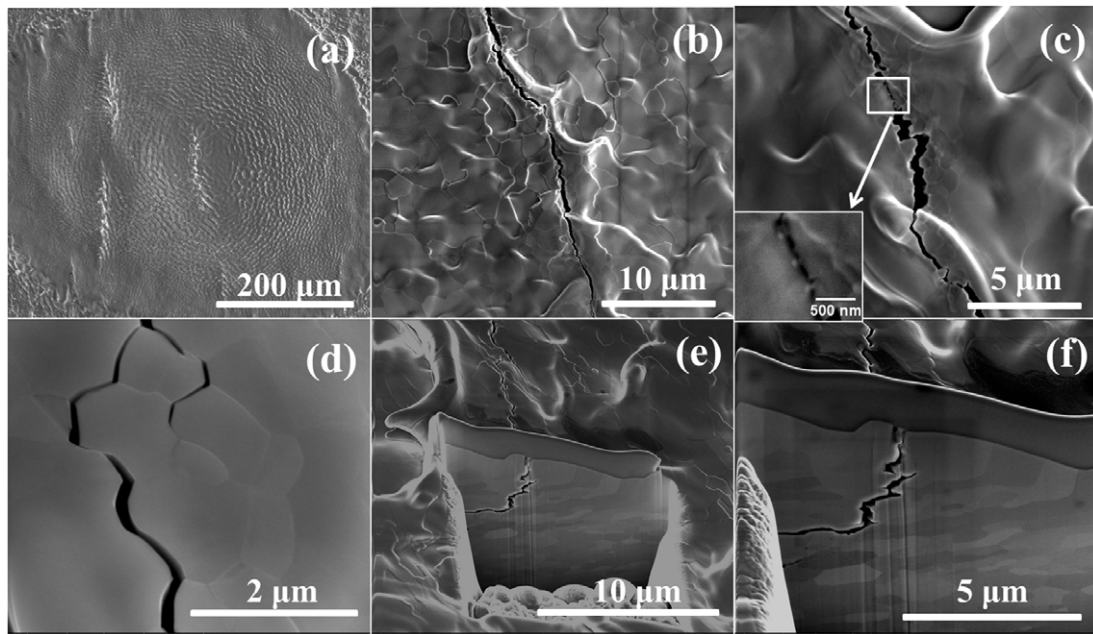
Figure 4. (*a*) Surface morphology of the W surface after irradiation with 50 pulses at $0.46\,\mathrm{MJ\,m^{-2}}$. (*b*) Crack near the molten region with a varying width that ranges from 150 to 550 nm. (*c*), (*d*) A zoomed region indicates that the crack occurred through a recrystallized region of ultrafine grains (<500 nm). (*e*), (*f*) Cross-section imaging of the cracks show a depth of a few micrometres in the middle of the molten region.
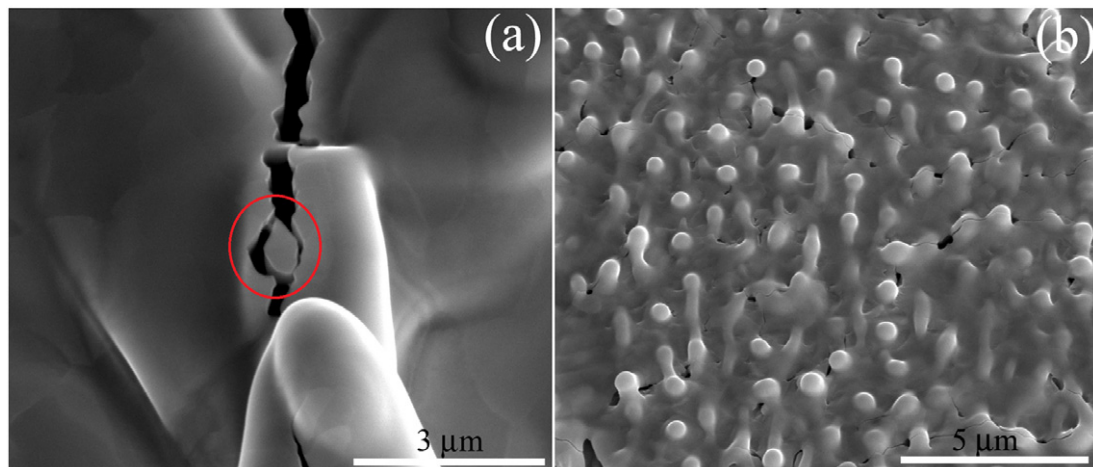

Figure 5. (*a*) Generation of particles inside the cracks produced on the tungsten surface, after 50 pulse exposures of $0.46\,\mathrm{MJ\,m^{-2}}$ and (*b*) SEM image of particles around the tungsten exposed surface with 50 pulses at $0.46\,\mathrm{MJ\,m^{-2}}$.

load that increases the dislocation density and the dislocation pile up on the boundaries of the ultrafine grains and thus induces a high level of residual stress. It is believed that embrittlement in tungsten is not an intrinsic property [30] but the interstitial impurities that are segregated at the grain boundaries [31, 32]. The segregated impurities on the grain boundaries render them weak links under mechanical straining and cause intergranular fracture [33, 34].

Particles with a size of a few micrometres were found inside the bulk cracks as shown in figures 4(*c*), (*d*) and 5(*a*). This concludes that the bulk cracks produce large particles and these results are consistent with large particle generation from the W surface under intense ion beam irradiation [21]. It is reported that the elastic energy stored in a stressed tungsten surface layer is responsible for generation of cracks, the main part of the elastic energy spent for cracking itself and the rest of the elastic energy remain after splitting the particle is transformed to the particle acceleration [21]. We believe that the fine cracks along the grain boundaries are responsible for the generation of small particles. Due to the exposure of the W surface with repetitive laser pulses, the delayed pulses interact with reconditioned target (melted and recrystallized). During the recrystallization of the surface, particles are loosely bounded at the grain boundaries. These loosely bounded particles are easily ejected during the irradiation of the next pulse. This makes the grain boundaries distinct and wider, resulting in their cracking, as given in figures 4(*c*) and (*d*). We estimated particle distribution and their sizes by placing a

silicon substrate at an angle of 20° with respect to the target normal and at a distance of 12 cm from the target surface. The AFM study of the deposited particles revealed that particles with hundreds of nanometre sizes were generated with a maximum probable size ∼50 nm diameter (figure not given). This is in good agreement with the SEM observation of some small particles in the vicinity of the crack (figure 4(c)).

In addition to the crack splashed particle observation, nanostructure formation (figure 5(b)) has been noticed in the laser-exposed W sample. Similar nanostructures were observed after high flux, high fluence He irradiation on tungsten by Kajita et al [35]. Under high particle irradiation load (such as the high flux He irradiation on tungsten by Kajita et al [35]), nanostructures were believed to occur due to helium bubble formation, growth and coalescence. Our results indicate that nanostructures on power loaded tungsten can even occur without the presence of He bubbles. We conjecture that the nanostructures formed in this study, however, are due to material diffusion to release the laser pulse induced residual and lateral stresses. Stress-driven surface diffusion was suggested to be a mechanism for nanostructure formation for metallic films exposed to oxygen plasma [36].

4. Conclusions

Tungsten target was exposed with repetitive pulses at $0.46\,\mathrm{MJ\,m^{-2}}$ energy loads from a high-power nanosecond laser. Intense particle emission was observed from the exposed W target and it started after a certain number of pulses. It has been concluded from the surface morphology characterization of treated surface that ductile-to-brittle transition of W is responsible for the generation of particles. Two types of cracks were observed on the treated surface; major cracks with 500 nm width and a network of fine grains around the grain boundaries with 200 nm width. Residual stresses are believed to be responsible for the bulk crack formation and large particles. Small particles are formed from the grain boundaries after the recrystallization of molten material. Our investigation showed the similarity in particle emission as well as surface morphology with the ion beam interaction with W target. Even though the power density used in this study is higher compared with the expected values in ITER, these results could be useful for the investigation of PFC erosion and material degradation during the abnormal events under ELM-like transients and high-energy loads.

Acknowledgments

References

[1] Philipps V. 2011 Tungsten as material for plasma-facing components in fusion devices *J. Nucl. Mater.* **415** S2–9

[2] Loarte A. *et al* 2007 Chapter 4: Power and particle control *Nucl. Fusion* **47** S203

[3] Miloshevsky G. and Hassanein A. 2013 Splashing and boiling mechanisms of melt layer losses of PFCs during plasma instabilities *J. Nucl. Mater.* **438** S155–9

[4] Hassanein A. and Sizyuk T. 2008 Comprehensive simulation of vertical plasma instability events and their serious damage to ITER plasma facing components *Nucl. Fusion* **48** 115008

[5] Neu R. *et al* 2005 Tungsten: an option for divertor and main chamber plasma facing components in future fusion devices *Nucl. Fusion* **45** 209

[6] Garkusha I.E. *et al* 2009 Experimental study of plasma energy transfer and material erosion under ELM-like heat loads *J. Nucl. Mater.* **390–391** 814–7

[7] Klimov N. *et al* 2009 Experimental study of PFCs erosion under ITER-like transient loads at plasma gun facility QSPA *J. Nucl. Mater.* **390–391** 721–6

[8] Brooks J.N. *et al* 2009 Plasma–surface interaction issues of an all-metal ITER *Nucl. Fusion* **49** 035007

[9] Winter J. 2000 Dust: a new challenge in nuclear fusion research? *Phys. Plasmas* **7** 3862–6

[10] Gierse N. *et al* 2011 *In situ* characterisation of hydrocarbon layers in TEXTOR by laser induced ablation and laser induced breakdown spectroscopy *J. Nucl. Mater.* **415** S1195–8

[11] Malaquias A. *et al* 2013 Development of ITER relevant laser techniques for deposited layer characterisation and tritium inventory *J. Nucl. Mater.* **438** S936–9

[12] Ivanova D. *et al* 2011 Laser-based and thermal methods for fuel removal and cleaning of plasma-facing components *J. Nucl. Mater.* **415** S801–4

[13] Huber A. *et al* 2011 Development of laser-based diagnostics for surface characterisation of wall components in fusion devices *Fusion Eng. Des.* **86** 1336–40

[14] Hai R. *et al* 2013 Laser-induced breakdown spectroscopic characterization of impurity deposition on the first wall of a magnetic confined fusion device: Experimental Advanced Superconducting Tokamak *Spectrochim. Acta* B **87** 147–52

[15] Bindhu C.V., Harilal S.S, Tillack M.S, Najmabadi F. and Gaeris A.C. 2004 Energy absorption and propagation in laser-created sparks *Appl. Spectrosc.* **58** 719–26

[16] Sizyuk T. and Hassanein A. 2013 Scaling of vapor/plasma shielding from laser produced plasmas to magnetic fusion regimes *Nucl. Fusion* submitted

[17] Linke J. *et al* 2001 Material degradation and particle formation under transient thermal loads *J. Nucl. Mater.* **290–293** 1102–6

[18] Linke J. *et al* 2000 High heat flux simulation experiments with improved electron beam diagnostics *J. Nucl. Mater.* **283–287** (Part 2) 1152–6

[19] Harilal S.S., Hassanein A. and Polek M. 2011 Late-time particle emission from laser-produced graphite plasma *J. Appl. Phys.* **110** 053301

[20] Amoruso S., Ausanio G., Bruzzese R., Vitiello M. and Wang X. 2005 Femtosecond laser pulse irradiation of solid targets as a general route to nanoparticle formation in a vacuum *Phys. Rev.* B **71** 033406

[21] Makhlaj V.A. *et al* 2013 Dust generation mechanisms under powerful plasma impacts to the tungsten surfaces in ITER ELM simulation experiments *J. Nucl. Mater.* **438** S233–6

[22] Greuner H. *et al* 2013 Investigation of European tungsten materials exposed to high heat flux H/He neutral beams *J. Nucl. Mater.* **442** S256–60

[23] Arzhannikov A.V. *et al* 2013 Surface modification and droplet formation of tungsten under hot plasma irradiation at the GOL-3 *J. Nucl. Mater.* **438** S677–80

[24] Klimov N. *et al* 2011 Experimental study of PFCs erosion and eroded material deposition under ITER-like transient loads at the plasma gun facility QSPA-T *J. Nucl. Mater.* **415** S59–64

[25] Bazylev B. *et al* 2009 Experimental and theoretical investigation of droplet emission from tungsten melt layer *Fusion Eng. Des.* **84** 441–5

[26] Wei Q. *et al* 2006 Microstructure and mechanical properties of super-strong nanocrystalline tungsten processed by high-pressure torsion *Acta Mater.* **54** 4079–89

[27] Garkusha I.E. *et al* 2005 Tungsten erosion under plasma heat loads typical for ITER type I ELMS and disruptions *J. Nucl. Mater.* **337–339** 707–11

[28] Hirai T., Pintsuk G., Linke J. and Batilliot M. 2009 Cracking failure study of ITER-reference tungsten grade under single pulse thermal shock loads at elevated temperatures *J. Nucl. Mater.* **390–391** 751–4

[29] Pestchanyi S.E. and Linke J. 2007 Simulation of cracks in tungsten under ITER specific transient heat loads *Fusion Eng. Des.* **82** 1657–63

[30] Lassner E. and Schubert W.D. 1999 *Tungsten: Properties, Chemistry, Technology of the Elements, Alloys, and Chemical Compounds* (Dordrecht/New York: Kluwer /Plenum)

[31] Wei Q. *et al* 2006 Mechanical behavior and dynamic failure of high-strength ultrafine grained tungsten under uniaxial compression *Acta Mater.* **54** 77–87

[32] Wei Q. *et al* 2005 Plastic flow localization in bulk tungsten with ultrafine microstructure *Appl. Phys. Lett.* **86** 101907

[33] Brosse J.B., Fillit R. and Biscondi M. 1981 Intrinsic intergranular brittleness of molybdenum *Scr. Metall.* **15** 619–23

[34] Thornley J.C. and Wronski A.S. 1969 The relation between the ductile–brittle transition temperature and grain size in polycrystalline molybdenum *Scr. Metall.* **3** 935–8

[35] Kajita S., Sakaguchi W., Ohno N., Yoshida N. and Saeki T. 2009 Formation process of tungsten nanostructure by the exposure to helium plasma under fusion relevant plasma conditions *Nucl. Fusion* **49** 095005

[36] El-Azab A. and Liang Y. 2003 Nanoscale copper oxide ring structure on an $SrTiO_3$ substrate *Phil. Mag.* **83** 3847–69